

Cite this: *J. Mater. Chem. A*, 2025, 13, 22604

Quasi-2D Ruddlesden–Popper perovskites with tunable wide bandgaps and phosphonium as additives for interface defect passivation in tandem solar cell design†

Qi Liu, Jian Jiang and Xiao Cheng Zeng *

Quasi-two-dimensional (Q2D) additive engineering has recently been demonstrated as an effective strategy for defect control and property enhancement in narrow-band-gap absorbers for high-efficiency perovskite tandem solar cells (*Nat. Energy*, 2022, 7, 642–651). In this study, we design a series of Q2D Ruddlesden–Popper perovskites incorporating phosphonium-based 2D additives, specifically $[\text{Ph}(\text{CH}_2)_2\text{PH}_3]_2\text{PbI}_4$ (abbreviated as PEP_2PbI_4), layer-stacked with $n\text{MAPbI}_3$ as a wide-band-gap absorber for perovskite tandem solar cell devices. First-principles calculations reveal that Q2D perovskites modified with PEP cations exhibit an approximately 0.2 eV wider bandgap compared to their phenylethylammonium (PEA) counterparts with the same layer thickness n . Certain thickness sequences are able to generate the energy funneling effect, resulting in the directional migration of carriers (*Adv. Mater.*, 2020, 32, 1906571). The larger terminal PEP cations introduce longer distances and more sharply tilt angles relative to the contact surface of bulk perovskite component $n\text{MAPbI}_3$, leading to distinct lattice matching properties and enhanced defect passivation when interfaced with charge transfer layers (CTLs). Additionally, PEP-functionalized Q2D perovskites demonstrate higher band offsets and larger work functions when interfaced with indium tin oxide (ITO) hole transport layers (HTLs), improving carrier extraction. Furthermore, the incorporation of PEP cations results in higher defect formation energies, effectively suppressing interface defect generation at the ITO contact. These findings highlight the potential of Q2D additive engineering to enhance both the stability and efficiency of wide-band-gap perovskites, offering a promising avenue for advancing perovskite-based tandem solar cells.

Received 17th March 2025
Accepted 29th May 2025DOI: 10.1039/d5ta02175h
rsc.li/materials-a

1 Introduction

Perovskite solar cells (PSCs) have emerged as a focal point in photovoltaic research over the past decade due to their exceptional power conversion efficiency (PCE), cost-effectiveness, ease of synthesis, and defect tolerance, among other advantages.^{1–3} The first perovskite-based solar cell, introduced by Miyasaka *et al.*,⁴ exhibited a modest PCE of 3.8%. However, rapid advancements in material engineering and device optimization have propelled the certified PCE of single-junction perovskite cells beyond 27.0% by now,⁵ fundamentally transforming photovoltaic material design and manufacturing strategies.

Phosphonium cations (PH_4^+ and its organic derivatives) exhibit chemical behavior similar to that of ammonium analogs but feature larger sizes and softer Lewis acidity.⁶ Recently,

phosphonium-based perovskites have attracted attention due to their unique optoelectronic characteristics.^{7,8} For example, Xiong *et al.* synthesized MPSnBr_3 (MP = methylphosphonium, CH_3PH_3^+ , $r_A = 2.50 \text{ \AA}$) with a wide bandgap of 2.62 eV, showing behavior similar to MASnBr_3 .^{9,10} Zhang *et al.* later reported ferroelectric and piezoelectric behavior associated with a large 2D phosphonium derivative, $(\text{EATMP})\text{PbBr}_4$.

Quasi-two-dimensional (Q2D) Ruddlesden–Popper (R–P) perovskites, composed of PbI_6^{4-} octahedra and large A-site cations such as PEA (phenylethylammonium) or BA (butylammonium), exhibit excellent environmental stability and defect tolerance due to their featured large-size hydrophobic organic terminals.^{11–13} Hou *et al.* highlighted that low-dimensional coatings stabilize the lattice and limit light-induced expansion, thereby improving device durability.¹⁴ Our previous work predicted that Q2D coatings can stabilize active MPSnBr_3 structures.¹⁵ Despite these advantages, 2D perovskite solar cells often suffer from reduced charge mobility and shorter carrier lifetimes compared to their 3D counterparts.¹⁶ However, by adjusting layer thickness, Q2D perovskites can offer bandgap gradients that enable energy funneling and

Department of Material Science and Engineering, City University of Hong Kong, Hong Kong SAR 999077, China. E-mail: xzeng26@cityu.edu.hk

† Electronic supplementary information (ESI) available. See DOI: <https://doi.org/10.1039/d5ta02175h>



directional carrier transfer procession.^{17–22} Riedl *et al.*²³ reported that anion segregation under illumination facilitates this funneling but also creates recombination-prone defects. Hou *et al.*¹⁴ also noted that illumination causes lattice stretching, altering the band structure.

Tandem solar cells offer higher PCE due to broader ranges of light absorption and efficient carrier separation.^{24,25} While conventional tandem cells adopt silicon, lattice mismatch introduces non-negligible interface defects.^{26–28} Perovskite-perovskite tandem cells can alleviate mismatches while enabling greener fabrication.^{29–33} Wide-bandgap absorbers, especially PEA-based Q2D layers, are promising due to their defect passivation and interface ordering.³⁴ However, necessary charge transfer layers introduce band offsets (BOs), which affect carrier transport.^{26,27,35–38} Positive BOs can enhance open-circuit voltage, while negative ones accelerate recombination. Similar to self-assembled monolayers (SAMs),^{39–41} Q2D perovskite surfaces also benefit from defect passivation.^{42–46} Nonetheless, studies on multilayer Q2D perovskites for tandem cell applications remain limited.^{47,48}

In this study, we designed a series of Q2D R-P layered phosphonium-based perovskites, PEP₂PbI₄·*n*MAPbI₃ (PEP = phenylethyl phosphonium cations, PhCH₂CH₂PH₃⁺), and investigated how their optoelectronic properties evolve with varying *n*-layer thickness (*n*). For comparison, we also examined their ammonium-based counterparts, PEA₂PbI₄·*n*MAPbI₃, to establish benchmarks. Furthermore, we explored an “energy funneling” carrier transfer mechanism by stacking Q2D perovskite layers with varied A-site cations and thicknesses. In addition, we analyzed carrier transfer processes between Q2D perovskites and CTLs, using ITO as a representative example. Lastly, we investigated defect-induced phenomena in PEP₂-PbI₄·*n*MAPbI₃ and PEA₂PbI₄·*n*MAPbI₃ with defect-containing CTL (ITO) surfaces. Our primary focus is on how these 2D-terminated structures mitigate CTL defects at the microscopic level through electronic structure analysis. By establishing a mechanistic framework and designing a model sequence of Q2D perovskite wide-bandgap absorbers, this study lays the groundwork for future experimental verification of the predicted mechanisms and potential applications of these materials in perovskite-to-perovskite tandem solar cells.

2 Computational details

First-principles density functional theory (DFT) calculations were performed with the Vienna *Ab Initio* Simulation Package (VASP 6.4)^{49–51} to study the geometric and electronic structures of all the 3D and Q2D perovskite series and their heterojunctions with CTLs. The projector augmented wave (PAW) pseudopotentials with a cutoff energy of 600 eV were employed. The generalized gradient approximation (GGA) exchange–correlation functional, Perdew–Burke–Ernzerhof (PBE),⁴⁸ with the DFT-D3 dispersion correction method of Grimme with zero damping^{52–54} was applied to optimize the geometrical structures. During the optimization of the geometries, all structures were allowed to relax until each atom was in mechanical equilibrium without any residual force >10^{−4} eV Å^{−1}.

We adopted a 20-angstrom vacuum slab for all the heterojunction structures to keep the structure largely isolated in the stacking direction. For systems involving interface defects, the vacuum layers were removed to prevent systematic errors generated by the charged vacuum layers. Since PBE computation usually underestimates the bandgaps of semiconductors, the more accurate HSE06 functional^{55,56} was adopted for the purpose of benchmark computation, particularly for electronic structures of the perovskite derivatives and the CTLs (excluding the heterointerfaces). Note that the HSE06 functional includes a fraction of screened Hartree–Fock exchange (as described by the parameter $\alpha = 0.2$) to improve the discontinuity of the derivative of the Kohn–Sham potential for integer electron numbers.

Moreover, the spin–orbit coupling (SOC) effect was taken into account in all the calculations except geometrical optimization. The electronic constituents for chemical elements involved in the DFT computations were 4d 5s 5p for Sn; 6s 5d 6p for Pb; 5p 6s for I, 2s 2p for B, C, N, and O; 3s 3p for P; 3d 4s for Ti; 4d 5p for In; and 1s for H. For all bulk systems, we adopted the PBE + SOC level of theory together with a 3 × 3 × 3 gamma-centered *k*-point grid generated by the Monkhorst–Pack scheme. For the perovskite heterojunctions, we used the PBE + SOC level of theory together with a 2 × 2 × 1 gamma-centered *k*-point grid. Due to the high computational cost of the HSE06 + SOC level of theory, gamma-only *k*-point mesh was adopted for computing the projected density of states (pDOS) of bulk systems.

To compute the electronic structure of the heterojunctions, a vacuum slab structure with identical stoichiometry and geometry along the *xy* plane (parallel to the interface) was employed to avoid unbalanced charges and excessive geometrical distortion. Additionally, the macroscopic average electrostatic potential method was undertaken to calculate the macroscopic average potential.^{57–61} The plane averaged potential on the heterojunction interface is given by: $\bar{V}(z) = 1/S \int \bar{V}(\vec{r}) dx dy$, where *S* represents the surface area of the interface. The bulk electrostatic average can be obtained from the following formula: $\bar{V}(z) = 1/L \int_{z-L/2}^{z+L/2} \bar{V}(\vec{z}) dz$, where *L* is the oscillation period of *V*(*z*). Based on the computed macroscopic average electrostatic potentials, the valence BO of the heterojunction can be calculated by using the formula: $\Delta E = \Delta \bar{V}_{\text{mix}} + (E_{\text{VBM,phaseA}} - E_{\text{VBM,phaseB}}) - (\Delta \bar{V}_{\text{phaseA}} - \Delta \bar{V}_{\text{phaseB}})$. Here, $\Delta \bar{V}_{\text{mix}}$ is the difference of *V*(*x*) at the interface, and the two terms in the parenthesis represent the valence band maximum (VBM) energy level difference and the potential difference, respectively, between the two different pure phases within the slab system.

The defect formation energies (DFEs) can be computed based on the formula⁶² $\text{DFE} = E_{\text{defected}} - (E_{\text{perfect}} + \sum \epsilon_{i,\text{dopants}}) + q(E_{\text{f}} + \text{VBM} + \Delta V_{\text{corr}}) + V_{\text{corr}}$,⁶² where *E_f* represents the Fermi-level, ΔV_{corr} means VBM potential differences between the defect-containing and pristine structures, and *q* denotes the charge state of a defect (for neutral defects, *q* = 0). *V_{corr}* is set for the electrostatic interaction correction between charged point defects in the periodically repeated supercells. In this work, the correction terms are neglected due to the inhomogeneity of the



heterojunction structures. The computation of DFEs allows an assessment of the relative likelihood for defect generation in equilibrium heterojunction structures and the relative stability of the different charge states of a given defect in the crystals.

3 Results and discussion

3.1 Structures and stabilities of Q2D layered perovskites $\text{PEP}_2\text{PbI}_4 \cdot n\text{MAPbI}_3$ with various thicknesses

We investigated how the Q2D perovskite $\text{PEP}_2\text{PbI}_4 \cdot n\text{MAPbI}_3$ and the PEA-based analog ($\text{PEA}_2\text{PbI}_4 \cdot n\text{MAPbI}_3$) vary with the thickness n . First, we adopted a monolayer coating of PEP or PEA cations on 3D MAPbI_3 as a benchmark, and the schematic diagrams are shown in Fig. 1. The fully optimized structures are displayed in Fig. S1 and S2,[†] and the corresponding geometric parameters are shown in Table 1.

As shown in Table 1, several geometric parameters of $\text{PEP}_2\text{PbI}_4 \cdot n\text{MAPbI}_3$ and the PEA-based analogs exhibit distinct trends as the thickness (n) increases. When $n = 0$, the Q2D perovskites adopt a 2D structure, forming PEP_2PbI_4 and PEA_2PbI_4 , which exhibit the greatest distortion and the longest Pb–I bond distances among the studied structures. As n increases, the Q2D perovskite framework transitions from monoclinic to orthorhombic with the corner-sharing MAPbI_3 fillings, becoming more flexible and resembling the 3D bulk structure of MAPbI_3 .

Furthermore, both the Pb–I bond lengths and $\angle \text{I–Pb–I}$ bond angles in PEP-based perovskites ($\text{PEP}_2\text{PbI}_4 \cdot n\text{MAPbI}_3$) exceed those in their PEA-based counterparts. Longer Pb–I bonds and larger $\angle \text{I–Pb–I}$ angles typically result in wider bandgaps and weaker band dispersion. Additionally, the SOC-induced band-splitting effect, which promotes indirect bandgap formation, is also diminished. Moreover, the “tilt angle” (Fig. 2) between the terminal A-site cations (PEA or PEP) and the xy plane of the PbI_6^{4-} framework differs significantly between the two Q2D layer-stacked structures. The larger size and softer Lewis acidity of PEP cations introduce greater distortion in the perovskite framework, leading to more sharply tilt angles. This structural distortion influences interface configurations and alters the electronic properties of the system.

To assess synthesis feasibility for the Q2D perovskites, we referred to the synthetic pathway reported in ref. 10, which could be adapted for phosphonium-bearing species.^{9,10} Specifically, we propose replacing CH_3I in the final quaternization step with $\text{PhCH}_2\text{CH}_2\text{I}$ (phenethyl iodide), followed by acid washing using concentrated HI to obtain the desired compound $[\text{PhCH}_2\text{CH}_2\text{PH}_3^+]\text{I}^-$ (PEPI). This synthesis pathway seems compatible with known procedures for making phosphonium halides, thereby providing a possible practical way for future experimental efforts. Following geometric relaxation, we calculated the formation energies (E_{form}) and phase segregation energies (E_{seg}) to evaluate the thermodynamic stability of PEP-

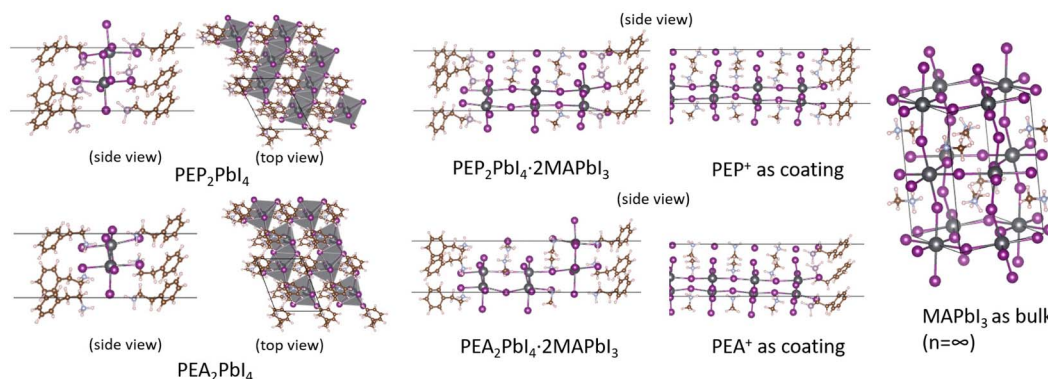


Fig. 1 Optimized structures of $\text{PEP}_2\text{PbI}_4 \cdot n\text{MAPbI}_3$ and $\text{PEA}_2\text{PbI}_4 \cdot n\text{MAPbI}_3$ with various thicknesses n . Further details are shown in Fig. S1 and S2[†].

Table 1 Optimized geometric parameters of the $[\text{PEP}_2\text{PbI}_4/\text{PEA}_2\text{PbI}_4] \cdot n\text{MAPbI}_3$ series as a function of thickness n^a

n	PEP					PEA					
	0	1	2	4	C	0	1	2	4	C	∞
$a/\text{\AA}$	8.37	8.44	8.55	8.58	8.58	7.80	8.17	8.22	8.46	8.48	7.83
$b/\text{\AA}$	10.13	10.08	9.90	9.88	9.92	9.50	10.05	9.96	9.82	9.89	9.48
α/deg	78.7	78.2	79.7	80.2	83.1	81.5	76.1	79.2	81.2	82.4	90.0
β/deg	90.6	91.8	92.5	91.3	90.6	90.8	91.6	92.2	90.7	90.0	89.6
Pb–I/ \AA	3.25	3.23	3.21	3.19	3.19	3.23	3.20	3.18	3.19	3.19	3.18
$\angle \text{I–Pb–I}/\text{deg}$	—	164.9	170.3	168.5	172.3	—	163.6	160.8	166.4	168.3	158.2
Tilt angle/ deg	55.6	56.5	57.3	56.9	59.2	64.8	65.1	64.9	63.9	65.3	—

^a Note that the C caption is for the single-terminal coating.



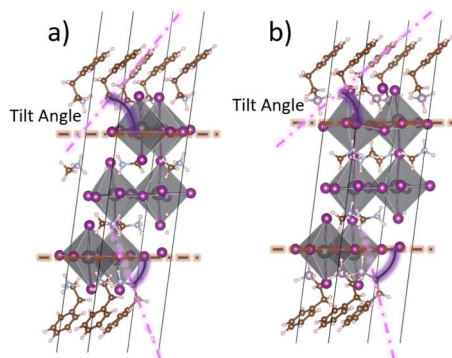


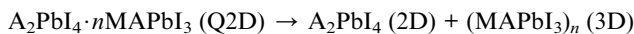
Fig. 2 Schematic diagram of the tilt angles in (a) $\text{PEA}_2\text{PbI}_4 \cdot n\text{MAPbI}_3$ and (b) $\text{PEP}_2\text{PbI}_4 \cdot n\text{MAPbI}_3$ with $n = 2$.

based perovskites, providing theoretical guidance for experimental synthesis.

The formation energy (E_{form}) was computed based on the reaction:



while the phase segregation energy (E_{seg}) was computed from the decomposition reaction:



As shown in Fig. 3a, the E_{form} of PEP-based perovskites displays a non-monotonic trend with increasing thickness parameter n : it initially increases, reaching a maximum at $n = 1$, and subsequently decreases. This behavior contrasts with that of PEA-based perovskites, where the formation energy decreases

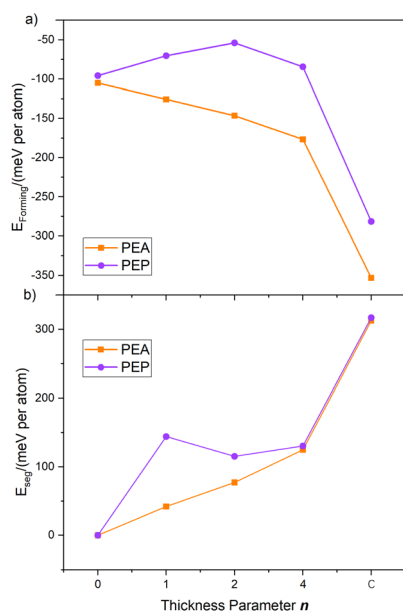


Fig. 3 (a) Formation energy (E_{form}) and (b) phase segregation energy (E_{seg}) of PEA and PEP-based perovskites versus thickness parameter n .

almost linearly with increasing thickness. The unusual trend seen for PEP-based systems is attributed to a structural rearrangement of the PbI_6^{4-} octahedra in the Q2D framework as n increases from 0 to 2. Specifically, while monolayer PEA_2PbI_4 adopts a planar 2D configuration, monolayer PEP_2PbI_4 , due to the larger size and lower polarity of the PEP cation, tends to form a quasi-1D linear chain-like structure (see Fig. 1). The transformation of the terminal layer from this chain-like motif to a planar configuration slightly reduces structural stability. Once a stable layered structure is established at higher n , the E_{form} of PEP-based Q2D perovskites resumes a more linear relationship with the thickness parameter.

Note that the thermodynamic stability of PEP-based perovskites is compromised, to a certain extent, by the weaker interaction between PEP and the perovskite surface. The P-H...I van der Waals interaction (H-I distance $\approx 2.70 \text{ \AA}$) is weaker compared to the N-H...I interaction in PEA-based systems (H-I distance $\approx 2.42 \text{ \AA}$), contributing to the less negative formation energies for PEP-containing structures than their PEA-based analogs.

In terms of phase segregation energy (Fig. 3b), PEP-terminated structures exhibit consistently higher E_{seg} values than their PEA counterparts, indicating a greater resistance to decomposition into separated A_2PbI_4 and bulk $(\text{MAPbI}_3)_n$ phases. This enhanced stability is attributed to the larger size and reduced polarity of the PEP cation, which allows the positively charged phosphorus center to penetrate more deeply into the $[\text{PbI}_6]^{4-}$ framework. Structural analysis reveals that the average Pb-I bond lengths in PEP-terminated surfaces are shorter (3.13 \AA in layered structures and 3.17 \AA in 2D monolayers) than those in their PEA-terminated counterparts (3.19 \AA and 3.35 \AA , respectively), suggesting stronger electrostatic interactions between the PEP cations and the perovskite lattice. These interactions help preserve the layered gradient structure while suppressing phase segregation, particularly in thinner configurations.

3.2 Band Structure of Q2D layered perovskites $\text{PEP}_2\text{PbI}_4 \cdot n\text{MAPbI}_3$ versus thickness n

We computed the band structures of the Q2D perovskite series, with Fig. 4 illustrating the predicted band gaps, work functions and effective carrier masses. The calculated optical properties are listed in Table 2, while the corresponding absorbance spectra are shown in Fig. 5. Additionally, Fig. S3† presents the computed structure and properties of bulk MAPbI_3 (corresponding to $n = \infty$). Notably, the bandgaps of the $\text{PEP}_2\text{PbI}_4 \cdot n\text{MAPbI}_3$ series decrease significantly as n increases, following a similar trend observed in the PEA-based analogs, in both PBE and HSE06 calculations (see Fig. 4a). For $n = 0$, the rigid 2D perovskites exhibit the largest bandgaps, with PEP-based systems displaying wider bandgaps than their PEA-based analogs. The most substantial bandgap reduction occurs when n increases from 0 to 1, after which the bandgap gradually declines, approaching that of the 3D bulk MAPbI_3 . Additionally, we checked how the work function (W_{f}) varied with n (see Fig. 4b and Table S1†). A notable work function gradient is shown with



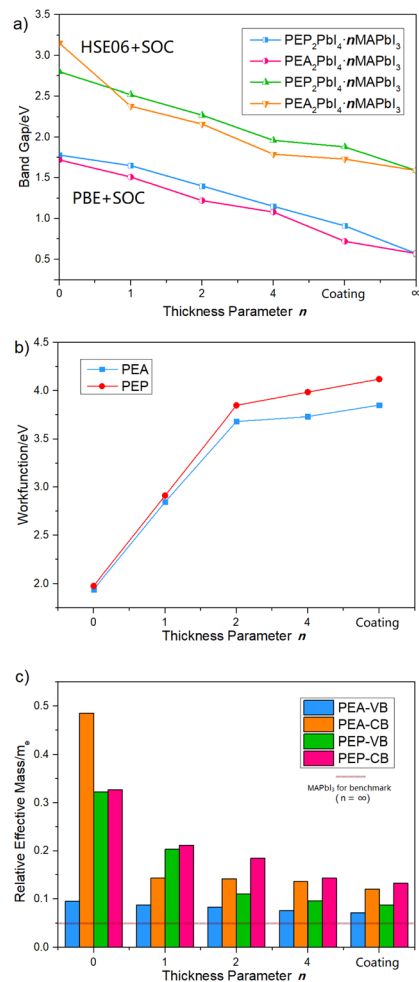


Fig. 4 Calculated (a) bandgaps, (b) work functions and (c) effective carrier masses of $\text{PEP}_2\text{PbI}_4 \cdot n\text{MAPbI}_3$ and $\text{PEA}_2\text{PbI}_4 \cdot n\text{MAPbI}_3$ with various thicknesses n at the PBE + SOC level of theory. Coating refers to the structures shown in Fig. 1

the increased thickness n . This thickness-dependent bandgap and work function modulation can be leveraged to achieve “energy funneling”,¹⁷ facilitating controlled charge transport *via* gradient thickness variations. The projected density of states (pDOS) for PEP- and PEA-containing Q2D perovskites at various thicknesses (n), computed using PBE + SOC, are shown in Fig. S4a and S5,† while those data obtained *via* HSE06 + SOC are shown in Fig. S6 and S7†.

A key characteristic of electron carriers in perovskites is their effective mass.^{63,64} The effective masses of carriers in the

Table 2 Calculated optical bandgap (OBG, in eV) and absorption peak (AP, in nm) of $\text{PEP}_2\text{PbI}_4 \cdot n\text{MAPbI}_3$ and $\text{PEA}_2\text{PbI}_4 \cdot n\text{MAPbI}_3$ as a function of thickness n at the HSE06 + SOC level of theory

n		0	1	2	4
OBG	$\text{PEP}_2\text{PbI}_4 \cdot n\text{MAPbI}_3$	2.62	2.11	1.89	1.86
	$\text{PEA}_2\text{PbI}_4 \cdot n\text{MAPbI}_3$	1.92	1.69	1.60	1.53
AP	$\text{PEP}_2\text{PbI}_4 \cdot n\text{MAPbI}_3$	363	451	503	512
	$\text{PEA}_2\text{PbI}_4 \cdot n\text{MAPbI}_3$	496	563	595	622

$\text{PEP}_2\text{PbI}_4 \cdot n\text{MAPbI}_3$ and $\text{PEA}_2\text{PbI}_4 \cdot n\text{MAPbI}_3$ series were determined by fitting the energy dispersions of the valence band maximum (VBM) and conduction band minimum (CBM) to quadratic functions, *i.e.*, $\frac{1}{m_{ii}^*} = \frac{1}{\hbar} \frac{\partial^2 E_n(k_i)}{\partial k_i^2}$ ($i = x, y$), where m_{xx} and m_{yy} correspond to the effective mass components along the x and y directions, respectively. The calculated effective masses, based on the band structures (Fig. S8†), are summarized in Fig. 4c. The Q2D PEP-based perovskites, which exhibit wider bandgaps, also possess higher carrier effective masses, leading to lower carrier mobility. Consequently, Q2D multilayer PEA-based perovskites, which demonstrate higher carrier activity, may enhance the efficiency of broadband absorbers.

As displayed in Fig. 5, Q2D PEP-based perovskites with smaller thicknesses exhibit an extended absorption range in the near-ultraviolet visible region, with absorption characteristics varying as a function of thickness (n), thereby enabling tunable absorption properties. Furthermore, carrier activity gradually increases with increasing n , with the CBM carrier activity being lower in PEA-based Q2D perovskites compared to their PEP-based analogs, while the opposite trend is observed for VBM carrier activity, except at $n = 0$ (see Fig. S8† for calculated band structures). Based on this trend, we propose a Q2D perovskite-based tandem subcell design in the form of ETL/PEP₂PbI₄·n₁-MAPbI₃/PEA₂PbI₄·n₂MAPbI₃/HTL, where $n_1 \leq n_2$, to achieve broad absorption and high carrier mobility.

In this suggested optimized tandem configuration, the PEP-based perovskite layers are directly connected to the electron transport layer (ETL) due to their higher CBM level and carrier activity, while the PEA-based layers are interfaced with the hole transport layer (HTL) owing to their higher VBM level and carrier activity. The condition $n_1 \leq n_2$ is essential for establishing a directional energy funnel through Q2D perovskite layer stackings of varying thicknesses, creating a band-gap gradient determined by both thickness and terminal cations. This gradient facilitates directional carrier migration, enhancing charge transport efficiency.

3.3 Carrier activities among $\text{PEP}_2\text{PbI}_4 \cdot n\text{MAPbI}_3$ and PEA-based analogs with charge transfer layers

In this section, we investigate the properties of combined structures by adding CTLs on the terminals of the Q2D

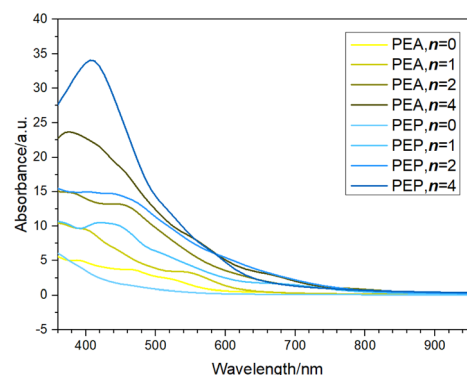


Fig. 5 Calculated absorption spectra of $\text{PEP}_2\text{PbI}_4 \cdot n\text{MAPbI}_3$ and $\text{PEA}_2\text{PbI}_4 \cdot n\text{MAPbI}_3$ series at the HSE06 + SOC level of theory.



perovskites to simulate a more realistic subcell within tandem solar cells. Here, we chose TiO_2 as the ETL and ITO (we adopt its dominant component In_2O_3 for calculation) as the HTL. The calculated pDOSs for the pristine CTLs are illustrated in Fig. S9,[†] calculated at both PBE and HSE06 + SOC levels of theory. Due to the significant lattice mismatch between the CTLs and the perovskite frameworks, we also employed larger supercells in our DFT computations. The data analysis for the latter scenario is based solely on the PBE + SOC level of theory. This heterojunction system consists of 4-layer CTLs and 3-layer perovskite frameworks, with a 20-angstrom vacuum layer introduced above the heterostructure. For the geometrical optimization, the two terminal layers adjacent to the vacuum layer were fixed, and their contributions were excluded from the electronic properties of the heterojunction system. Consequently, the minimum common multiple supercell crystal planes exhibited a lattice mismatch of less than 3%.

Both three-dimensional (3D) and Q2D perovskite systems were considered in our analysis. The 3D perovskite was aligned with the HTL at the (110) orientation, while the Q2D perovskite was oriented with the A-site facing the CTLs. We computed the interface binding energies and interface distances (IDs), defined as the smallest distance from the CTL terminals to the perovskite's PbI_6^{4-} frameworks (see Tables S2 and S3[†]). The optimized interfaces for perovskite/ TiO_2 are shown in Fig. S10,[†] and the optimized interfaces for perovskite/ITO are presented in Fig. S11.[†]

Our findings reveal that the surface binding energy of PEA-terminated Q2D perovskite is lower than that of PEP, regardless of whether the surface contact is with TiO_2 or ITO. Although PEP cations exhibit smaller tilt angles on the perovskite surface, PEP-coated Q2D perovskites show larger IDs with the adjacent CTLs due to the greater size of PEP ($d_{\text{P-H}} = 1.42$ angstroms) compared to PEA (see Table 3). This discrepancy explains why the PEA terminal demonstrates lower surface energy, influencing its response to CTL interface defects (see Section 3.4 below). With the 2D organic cation coating, the PbI_6^{4-} octahedral layer of the perovskite is no longer in direct contact with the CTLs (either TiO_2 or ITO) but is instead separated by the 2D PEP or PEA cations. This separation reduces the direct interaction between the mismatched lattices, leading to efficient interface passivation, as indicated by the elongated ID.

Due to the significant lattice matching ratio between the Q2D (PEP/PEA) $_2\text{PbI}_4$ series and the TiO_2 electron transport layer (ETL) (see Table 4), accurately predicting the electronic structure of their heterointerface in such huge supercells exceeds the computational limits of our facility. Therefore, we focus solely on the heterointerface system involving In_2O_3 (ITO) (x orientation) as the HTL for electronic structure calculations.

Table 4 Supercell matching ratio of 3D and Q2D perovskites to CTLs (ETL or HTL)

CTL orientation	ETL (TiO_2)		HTL (ITO)	
	x	y	x	y
3D MAPbI_3	2 : 3	2 : 5	1 : 1	2 : 3
Q2D $\text{PEP}(\text{PEA})_2\text{PbI}_4$	4 : 5	3 : 4	2 : 3	3 : 5

The calculated valence band BOs are +0.33 eV for the MA/ITO interface, +0.64 eV for PEA/ITO, and +0.51 eV for the PEP/ITO interface (see Fig. S12a and b[†]). This means that PEA cations as perovskite coatings suppress carrier non-radiative recombination better than their phosphonium derivative PEP. Meanwhile, the computed work functions (see Fig. S12c and Table S4[†]) show that the PEP-terminated perovskite is slightly superior to PEA homologs in terms of work function regulation due to PEP's larger size and stronger surface distortions evidenced by its smaller tilt angles. Therefore, we propose that if $\text{PEP}_2\text{-PbI}_4 \cdot n\text{MAPbI}_3$ was adopted as a wide-bandgap absorber, $\text{PEA}_2\text{-PbI}_4 \cdot n\text{MAPbI}_3$ with similar thickness n can be coated on the PEP homologs as an isomorphic layer to improve the structural stability while increasing carrier lifetimes owing to PEA's higher binding energies and larger BOs at the ITO surface.

Given that PEP-based Q2D perovskites exhibit wider bandgaps and broader absorption ranges, we suggest utilizing the narrower-bandgap PEA homologs as an intermediate transition layer. This approach offers two key benefits: improved surface stability by mitigating lattice mismatch and enhanced charge carrier transport through energy funneling. If the thickness parameter n remains identical between the two layers, the narrower-bandgap PEA domains will preferentially attract charge carriers, reducing energy loss from non-radiative recombination or phonon interactions. This design strategy for Q2D-based wide-bandgap subcells to build tandem cells can be summarized as $\text{ETL}/\text{PEP}_2\text{PbI}_4 \cdot n_1\text{MAPbI}_3/\text{PEA}_2\text{PbI}_4 \cdot n_2\text{MAPbI}_3/\text{HTL}$, $n_1 \leq n_2$. A schematic carrier transfer diagram based on such a design is shown in Fig. 6, as well as the larger PEP cations tend to promote the formation of thinner Q2D structures.⁶⁵

3.4 Defect passivation within MA, PEA, and PEP perovskite terminals and ITO interface

Heterojunction defect-induced behaviors play a crucial role in carrier transition processes between the perovskite absorber and CTLs. To achieve favorable band-gap alignment with the wide band perovskite stacks, we selected a wide-bandgap MA-based perovskite, MAPbBr_2Cl , rather than the narrower-bandgap MAPbI_3 . According to HSE06 + SOC computations,

Table 3 Calculated interface binding energy (in $\text{meV } \text{\AA}^{-2}$) and interface distance (in angstrom) of 3D and Q2D perovskites to CTLs (ETL or HTL)

CTL perovskite terminals	ETL (TiO_2)			HTL (ITO)		
	MA	PEA	PEP	MA	PEA	PEP
Binding energy ($\text{meV } \text{\AA}^{-2}$)	-43.6	-37.2	-29.9	-155.3	-72.9	-71.5
Interface distance (\AA)	2.73	7.60	7.69	3.28	8.16	8.76



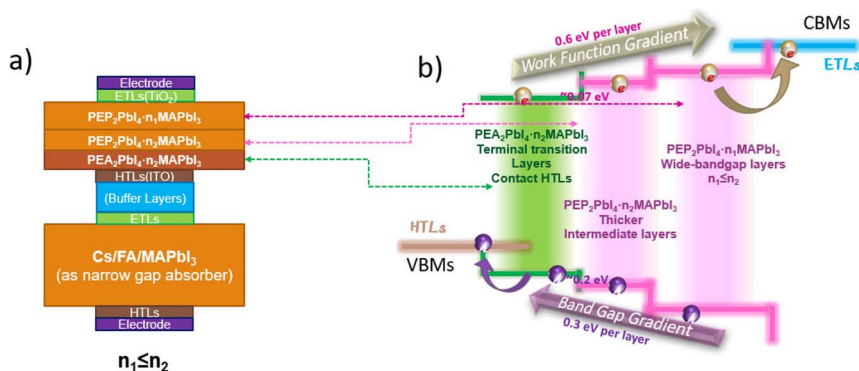


Fig. 6 Schematic diagrams of (a) the Q2D perovskite subcell for tandem-cell devices and (b) the predicted carrier transfer pathway through this subcell. The left brown bar refers to the VBM of HTL while the right blue bar refers to the CBM or ETL; the bandgaps of three Q2D perovskite layers in the upper panel of (a) are illustrated, correspondingly, in (b).

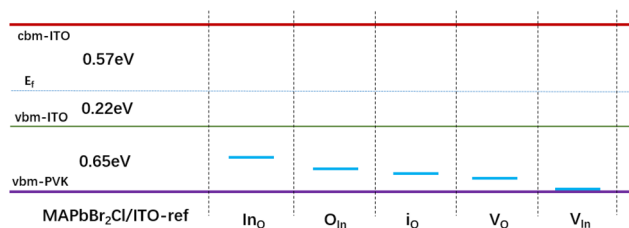


Fig. 7 Schematic diagram of the trap states due to the defect-containing 3D MAPbBr₂Cl/ITO interface structures based on Fig. S15 and S16.† "PVK" refers to "perovskite layers". The p-type defects considered here include the antisites In_o, O_{In}, oxygen and indium vacancies V_O and V_{In}, and the interstitial oxide i_o on the ITO layer.

MAPbBr₂Cl has a bandgap of 3.15 eV, making it a suitable benchmark for investigating the electronic properties of perovskite/HTL systems with defective HTLs. Fig. S13, S14 and Table S5† present the calculated geometric and electronic properties. To eliminate systematic errors caused by the presence of a charged vacuum layer, we excluded vacuum layers from the subsequent analysis. Since the VASP6.4 package cannot handle charged vacuum layers properly, we do not take into account charged situations in the vacuum-slab structures. In other words, all defects are considered neutral.

The optimized structures used for defect formation energy and electronic structure calculations are depicted in Fig. S17,† while Fig. S16† illustrates the optimized structure of MAPbBr₂Cl/ITO with defects on the ITO layer. The projected density of states (pDOS) for MAPbBr₂Cl/ITO with ITO defects is

Table 5 Calculated defect formation energy (DFE, in eV) of 3D MAPbBr₂Cl and Q2D PEA/PEP-terminal MAPbI₃ perovskites with the various categories of defects (neutral) on the ITO layer

Defect categ.	In _o	O _{In}	i _o	V _O	V _{In}
MAPbBr ₂ Cl	0.958	0.770	0.026	4.536	3.451
PEA-ter. MAPbI ₃	0.319	1.731	0.531	0.809	3.401
PEP-ter. MAPbI ₃	-0.009	1.799	1.769	0.421	4.6013

shown in Fig. S17,† and a schematic representation of the trapping states is provided in Fig. 7.

Based on the DFEs and IDs shown in Tables 5 and S6,† we conclude that the PEP coatings exhibit stronger suppression of defect formation than their PEA counterparts due to the higher DFEs in most types of defects. This advantage arises from PEP's larger molecular size and reduced tilt angle within the perovskite framework (see Fig. S18 and S19†). However, the pronounced p-type electronic nature of PEP coatings compromises their passivation capability.

In conventional 3D perovskite structures interfaced with defective ITO layers, p-type defects significantly disrupt carrier transport paths (see Fig. 7). When PEA-terminated Q2D perovskites are used, only two antisite defects—In_o and O_{In}—generate trap states, as illustrated in Fig. 8 and supported by the pDOS calculations (Fig. S20 and S21†). In contrast, PEP-terminated Q2D perovskites exhibit three types of carrier traps: In_o, O_{In} and V_{In}, suggesting a more substantial impact on charge transport,

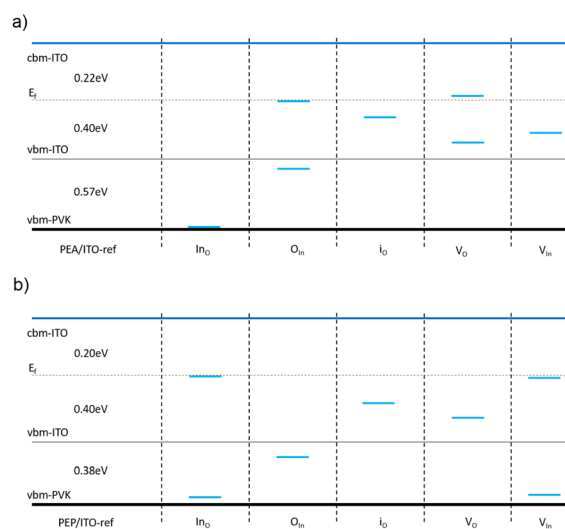


Fig. 8 Schematic diagrams of the trap states due to the defect-containing ITO structures with the interface of Q2D (a) PEA-terminated and (b) PEP-terminated MAPbI₃ perovskites.



especially In₂O₃, which shows lower DFE than PEA analogs. Despite these differences, both Q2D terminal cations significantly reduce surface defect density in ITO layers by increasing defect formation energy and minimizing disruptions to the electronic structure and carrier transport pathways. Among the two, PEP coatings offer superior passivation due to their higher defect formation energy and fewer trap states during carrier transfer.

4 Conclusion

In this study, we explored a series of Q2D perovskites, PEP₂-PbI₄·*n*MAPbI₃, for potential application in tandem solar cells, as these Q2D perovskites likely offer tunable wide bandgaps, improved carrier transport, and enhanced defect passivation. The introduction of large PEP cations not only widens the bandgap by 0.2 eV compared to PEA-based analogs, thereby benefiting visible spectrum absorption, but also enables energy funneling through controlled thickness variation of *n*MAPbI₃.

The inclusion of Q2D organic cations at the perovskite-CTL interface prevents direct contact between the PbI₆⁴⁻ octahedra and CTLs such as ITO. PEP cations, with their sharpened tilt angles, reduce lattice mismatch more effectively than their PEA counterparts. Conversely, PEA coatings, despite larger work-function differences, exhibit stronger carrier activity and help establish carrier migration gradients across heterostructure interfaces. As a result, PEA-based Q2D layers can serve as transitional buffers between wide bandgap PEP perovskites and CTLs.

Additionally, the Q2D cations can help to address defect-related challenges at the ITO surface, particularly near the valence band maximum. While PEP-coated films show higher formation energies for certain p-type defects, PEA-coated layers can result in improved passivation. In contrast, direct contact between 3D perovskites and defective oxide CTLs promotes low-energy defect formation, thereby hindering efficient carrier transport.

Finally, we propose that using PEP₂PbI₄·*n*₁ MAPbI₃ as a wide-band-gap absorber, combined with an isomorphic PEA₂PbI₄·*n*₂ MAPbI₃ (*n*₁ ≤ *n*₂) intermediate transition layer between the absorber and HTL (e.g., ITO), holds significant potential for improving tandem solar cell performance. We anticipate that future experimental validation of this design principle could lead to highly efficient tandem devices.

Data availability

The data supporting this article have been included as part of the ESI.†

Author contributions

Q. L. handled the DFT computations under the supervision of X. C. Z. Both J. J. and X. C. Z. provided the funding.

Conflicts of interest

The authors declare that they have no known competing financial interests or personal relationships that could have appeared to influence the research project reported in this paper.

Acknowledgements

J. J. acknowledges the funding support from the National Natural Science Foundation of China (Grant No. 22303072), X. C. Z. acknowledges the support by the Hong Kong Global STEM Professorship Scheme and the Research Grants Council of Hong Kong Grant (C1055-23G and CRS Cityu 104/24).

References

- 1 A. Jena, A. Kulkarni and T. Miyasaka, *Chem. Rev.*, 2019, **119**, 3036–3103.
- 2 S. D. Stranks and H. J. Snaith, *Nat. Nanotechnol.*, 2015, **10**, 391–402.
- 3 M. Grätzel, *Nat. Mater.*, 2014, **13**, 838–842.
- 4 A. Kojima, K. Teshima, Y. Shirai and T. Miyasaka, *J. Am. Chem. Soc.*, 2009, **131**, 6050–6051.
- 5 National Renewable Energy Laboratory, *Best Research-Cell Efficiencies*, 2025, available at <https://www.nrel.gov/pv/cell-efficiency>.
- 6 *Das Periodensystem der Elemente* online, 2023, available at <https://web.archive.org/web/20181116050427/>, <http://www.periodensystem-online.de/index.php>.
- 7 G. Kieslich, S. Sun and A. K. Cheetham, *Chem. Sci.*, 2015, **6**, 3430–3433.
- 8 S. Körbel, M. A. L. Marques and S. Botti, *J. Mater. Chem. A*, 2018, **6**, 6463–6475.
- 9 H.-Y. Zhang, Z.-X. Zhang, X.-G. Chen, X.-J. Song, Y. Zhang and R.-G. Xiong, *J. Am. Chem. Soc.*, 2021, **143**, 1664–1672.
- 10 H.-Y. Zhang, X.-G. Chen, Z.-X. Zhang, X.-J. Song, T. Zhang, Q. Pan, Y. Zhang and R.-G. Xiong, *Adv. Mater.*, 2020, **32**, 2005213.
- 11 C. M. Perez, D. Ghosh, O. Prezhdo, W. Nie, S. Tretiak and A. Neukirch, *J. Phys. Chem. Lett.*, 2022, **13**, 5213–5219.
- 12 S. Li, Z. Zheng, J. Ju, S. Cheng, F. Chen, Z. Xue, L. Ma and Z. Wang, *Adv. Mater.*, 2024, **36**, 2307701.
- 13 F. Pei, Y. Chen, Q. Wang, L. Li, Y. Ma, H. Liu, Y. Duan, T. Song, H. Xie, G. Liu, N. Yang, Y. Zhang, W. Zhou, J. Kang, X. Niu, K. L. F. Wang, M. Xiao, G. Yuan, Y. Wu, C. Zhu, X. Wang, H. Zhou, Y. Wu and Q. Chen, *Nat. Commun.*, 2024, **15**, 7024.
- 14 Q. Li, Y. Zheng, H. Wang, X. Liu, M. Lin, X. Sui, X. Leng, D. Liu, Z. Wei, M. Song, D. Li, H. G. Yang, S. Yang and Y. Hou, *Science*, 2025, **387**, 1069–1077.
- 15 Q. Liu, M.-G. Ju and X. C. Zeng, *Materials Today Energy*, 2024, **42**, 101556.
- 16 Y. Huang, T. Liu, D. Li, D. Zhao, A. Amini, C. Cheng and G. Xing, *Nano Energy*, 2021, **88**, 106219.
- 17 A. M. Oddo, M. Gao, D. Weinberg, J. Jin, M. C. Folgueras, C. Song, C. Ophus, T. Mani, E. Rabani and P. Yang, *Nano Lett.*, 2023, **23**, 11469–11476.
- 18 L. N. Quan, M. Yuan, R. Comin, O. Voznyy, E. M. Beauregard, S. Hoogland, A. Buin, A. R. Kirmani, K. Zhao, A. Amassian, D. H. Kim and E. H. Sargent, *J. Am. Chem. Soc.*, 2016, **138**, 2649–2655.
- 19 M. Yuan, L. Quan, R. Comin, *et al.*, *Nat. Nanotechnol.*, 2016, **11**, 872–877.



- 20 J. Liu, J. Leng, K. Wu, J. Zhang and S. Jin, *J. Am. Chem. Soc.*, 2017, **139**, 1432–1435.
- 21 L. Lei, D. Seyitliyev, S. Stuard, J. Mendes, Q. Dong, X. Fu, Y.-A. Chen, S. He, X. Yi, L. Zhu, C.-H. Chang, H. Ade, K. Gundogdu and F. So, *Adv. Mater.*, 2020, **32**, 1906571.
- 22 N. Zhou, Y. Shen, L. Li, S. Tan, N. Liu, G. Zheng, Q. Chen and H. Zhou, *J. Am. Chem. Soc.*, 2018, **140**, 459–465.
- 23 K. O. Brinkmann, P. Wang, F. Lang, W. Li, X. Guo, F. Zimmermann, S. Olthof, D. Neher, Y. Hou, M. Stolterfoht, T. Wang, A. B. Djuricic and T. Riedl, *Nat. Rev. Mater.*, 2024, **9**, 202–217.
- 24 H. Li and W. Zhang, *Chem. Rev.*, 2020, **120**, 9835–9950.
- 25 J. Kromdijk, K. Glowacka, L. Leonelli, S. T. Gabilly, M. Iwai, K. K. Niyogi and S. P. Long, *Science*, 2016, **354**, 857–861.
- 26 K. Bush, A. Palmstrom and Z. e. a. Yu, *Nat. Energy*, 2017, **2**, 17009.
- 27 J. Werner, B. Niesen and C. Ballif, *Adv. Mater. Interfaces*, 2018, **5**, 1700731.
- 28 M. T. Horantner and H. J. Snaith, *Energy Environ. Sci.*, 2017, **10**, 1983–1993.
- 29 F. Jiang, T. Liu, B. Luo, J. Tong, F. Qin, S. Xiong, Z. Li and Y. Zhou, *J. Mater. Chem. A*, 2016, **4**, 1208–1213.
- 30 J. H. Heo and S. H. Im, *Adv. Mater.*, 2016, **28**, 5121–5125.
- 31 D. P. McMeekin, G. Sadoughi, W. Rehman, G. E. Eperon, M. Saliba, M. T. Horantner, A. Haghighirad, N. Sakai, L. Korte, B. Rech, M. B. Johnston, L. M. Herz and H. J. Snaith, *Science*, 2016, **351**, 151–155.
- 32 B. Chen, Z. Yu, A. Onno, Z. Yu, S. Chen, J. Wang, Z. C. Holman and J. Huang, *Sci. Adv.*, 2022, **8**, eadd0377.
- 33 Z. Song, C. Chen, C. Li, R. A. Awni, D. Zhao and Y. Yan, *Semicond. Sci. Technol.*, 2019, **34**, 093001.
- 34 A. Rajagopal, R. J. Stoddard, S. B. Jo, H. W. Hillhouse and A. K.-Y. Jen, *Nano Lett.*, 2018, **18**, 3985–3993.
- 35 S. Abdelaziz, A. Zekry, A. Shaker and M. Abouelatta, *Opt. Mater.*, 2022, **123**, 111893.
- 36 H. Hu, S. Moghadamzadeh, R. Azmi, Y. Li, M. Kaiser, J. C. Fischer, Q. Jin, J. Maibach, I. M. Hossain, U. W. Paetzold and B. Abdollahi Nejjand, *Adv. Funct. Mater.*, 2022, **32**, 2107650.
- 37 C. Ding, Y. Zhang, F. Liu, Y. Kitabatake, S. Hayase, T. Toyoda, K. Yoshino, T. Minemoto, K. Katayama and Q. Shen, *Nano Energy*, 2018, **53**, 17–26.
- 38 T. Minemoto and M. Murata, *Sol. Energy Mater. Sol. Cells*, 2015, **133**, 8–14.
- 39 Z. Dai, S. K. Yadavalli, M. Chen, A. Abbaspourtamijani, Y. Qi and N. P. Padture, *Science*, 2021, **372**, 618–622.
- 40 I. Levine, A. Al-Ashouri, A. Musienko, H. Hempel, A. Magomedov, A. Drevilkauskaitė, V. Getautis, D. Menzel, K. Hinrichs, T. Unold, S. Albrecht and T. Dittrich, *Joule*, 2021, **5**, 2915–2933.
- 41 S. Y. Kim, S. J. Cho, S. E. Byeon, X. He and H. J. Yoon, *Adv. Energy Mater.*, 2020, **10**, 2002606.
- 42 J.-H. Kim, C.-M. Oh, I.-W. Hwang, J. Kim, C. Lee, S. Kwon, T. Ki, S. Lee, H. Kang, H. Kim and K. Lee, *Adv. Mater.*, 2023, **35**, 2302143.
- 43 D. S. Lee, J. S. Yun, J. Kim, A. M. Soufiani, S. Chen, Y. Cho, X. Deng, J. Seidel, S. Lim, S. Huang and A. W. Y. Ho-Baillie, *ACS Energy Lett.*, 2018, **3**, 647–654.
- 44 G. Jin, T. Liu, Y. Li, J. Zhou, D. Zhang, P. Pang, Z. Ye, Z. Xing, G. Xing, J. Chen and D. Ma, *Nanoscale*, 2022, **14**, 919–929.
- 45 W. Dong, H. Li, J. Li, Y. Hua, F. Yang, Q. Dong, X. Zhang and W. Zheng, *Nano Lett.*, 2024, **24**, 3952–3960.
- 46 G. Liu, X.-X. Xu, S. Xu, L. Zhang, H. Xu, L. Zhu, X. Zhang, H. Zheng and X. Pan, *J. Mater. Chem. A*, 2020, **8**, 5900–5906.
- 47 D. H. Kim, C. P. Muzzillo, J. Tong, A. F. Palmstrom, B. W. Larson, C. Choi, S. P. Harvey, S. Glynn, J. B. Whitaker, F. Zhang, Z. Li, H. Lu, M. F. van Hest, J. J. Berry, L. M. Mansfield, Y. Huang, Y. Yan and K. Zhu, *Joule*, 2019, **3**, 1734–1745.
- 48 Y. Huang, T. Liu, D. Li, D. Zhao, A. Amini, C. Cheng and G. Xing, *Nano Energy*, 2021, **88**, 106219.
- 49 G. Kresse, *J. Non-Cryst. Solids*, 1995, **193**, 222–229.
- 50 P. E. Blöchl, *Phys. Rev. B: Condens. Matter Mater. Phys.*, 1994, **50**, 17953–17979.
- 51 J. P. Perdew, K. Burke and M. Ernzerhof, *Phys. Rev. Lett.*, 1996, **77**, 3865–3868.
- 52 S. Grimme, *J. Comput. Chem.*, 2006, **27**, 1787–1799.
- 53 S. Grimme, J. Antony, S. Ehrlich and H. Krieg, *J. Chem. Phys.*, 2010, **132**, 154104.
- 54 J. Moellmann and S. Grimme, *J. Phys. Chem. C*, 2014, **118**, 7615–7621.
- 55 J. Heyd and G. E. Scuseria, *J. Chem. Phys.*, 2004, **120**, 7274.
- 56 J. Heyd, G. E. Scuseria and M. Ernzerhof, *J. Chem. Phys.*, 2003, **118**, 8207.
- 57 A. Baldereschi, S. S. Baroni and R. Resta, *Phys. Rev. Lett.*, 1988, **61**, 1734–1737.
- 58 Z. H. Wang, M. W. Zhao, X. P. Wang, Y. Xi, X. J. He, X. G. Liu and S. S. Yan, *Phys. Chem. Chem. Phys.*, 2012, **14**, 15693–15698.
- 59 Y. C. Fan, K. Y. Hou, Z. H. Wang, T. He, X. Zhang, H. Zhang, J. Dong, X. Liu and M. W. Zhao, *J. Phys. D: Appl. Phys.*, 2011, **44**, 095405.
- 60 N. R. D'Amico, G. Cantele and D. Ninno, *Appl. Phys. Lett.*, 2012, **101**, 141606.
- 61 Y. Sun, L. Luan, J. Zhao, Y. Zhang, X. Wei, J. Fan, L. Ni, C. Liu, Y. Yang, J. Liu, Y. Tian and L. Duan, *Mater. Sci. Semicond. Process.*, 2023, **168**, 107822.
- 62 D. Meggiolaro and F. D. Angelis, *ACS Energy Lett.*, 2018, **3**, 2206–2222.
- 63 M. G. Ju, G. X. Sun, Y. Zhao and W. Z. Liang, *Phys. Chem. Chem. Phys.*, 2015, **17**, 17679–17687.
- 64 J. Feng and B. Xiao, *J. Phys. Chem. C*, 2014, **118**, 19655–19660.
- 65 H. Gu, J. Xia, C. Liang, Y. Chen, W. Huang and G. Xing, *Nat. Rev. Mater.*, 2023, **8**, 533–551.

